Supplemental Materials for "Pressure-Induced Split of the Density Wave Transitions in $La_3Ni_2O_{7-\delta}$"

Rustem Khasanov,[1,*] Thomas J. Hicken,[1] Dariusz J. Gawryluk,[2] Steffen Bötzel,[3]
Frank Lechermann,[3] Ilya M. Eremin,[3] Hubertus Luetkens,[1] and Zurab Guguchia[1]

[1] *Laboratory for Muon Spin Spectroscopy, Paul Scherrer Institut, CH-5232 Villigen PSI, Switzerland*
[2] *Laboratory for Multiscale Materials Experiments, Paul Scherrer Institut, CH-5232 Villigen PSI, Switzerland*
[3] *Theoretische Physik III, Ruhr-Universität Bochum, D-44780 Bochum, Germany*

I. SAMPLE PREPARATION AND CHARACTERIZATION

Polycrystalline $La_3Ni_2O_{7-\delta}$ was obtained combining mechanosynthesis at 12 bar of oxygen pressure and solid-state reaction in oxygen flow. Freshly dried La_2O_3 (5N, Sigma-Aldrich) and NiO (4N8, Alfa Aesar) were used as starting materials. Stoichiometric amounts of raw oxides (5 g in total) were initially grounded during 20 cycles with 750 rpm for 5 min milling and 5 min cooling conditions in a PULVERISETTE 7 planetary micro ball-mill (Fritsch GmbH). Resulting fine black powder was cold-pressed into a pellet and annealed at 1250°C for 60 h in 100 ml/min oxygen flow. Annealing process at 1250°C was repeated 3 times with intermediate regrinding and repelletizing. Final thermal treatment in oxygen flow was performed at 500°C for 12 h. Resulting samples were tested by means of laboratory powder x-ray diffraction experiments performed at room temperature (RT) in the Bragg-Brentano geometry using a Bruker AXS D8 Advance diffractometer (Bruker AXS GmbH, Karlsruhe, Germany) equipped with a Ni-filtered Cu Kα radiation and a 1D LynxEye PSD detector. Rietveld analysis of obtained diffractograms was subsequently performed,[1] utilizing FullProf Suite package.[2] Refined unit cell parameters of the orthorhombic $La_3Ni_2O_{7-\delta}$ phase, $a = 5.39481(2)$, $b = 5.44999(2)$, and $c = 20.5368(1)$ Å, are in very good agreement with previously reported data for polycrystalline oxygen stoichiometric phase ($\delta \simeq 0.0$).[3–5] In addition to the main phase, we have observed $\simeq 8$ % of lanthanum silica apatite,[6] which appearance may be attributed to utilized agate setup for ball milling. We have not noticed any particular changes in crystallinity, phase purity or lattice parameters over each applied annealing procedure steps.

X-ray diffraction patterns of polycrystalline $La_3Ni_2O_{7-\delta}$ are presented in Figure 1.

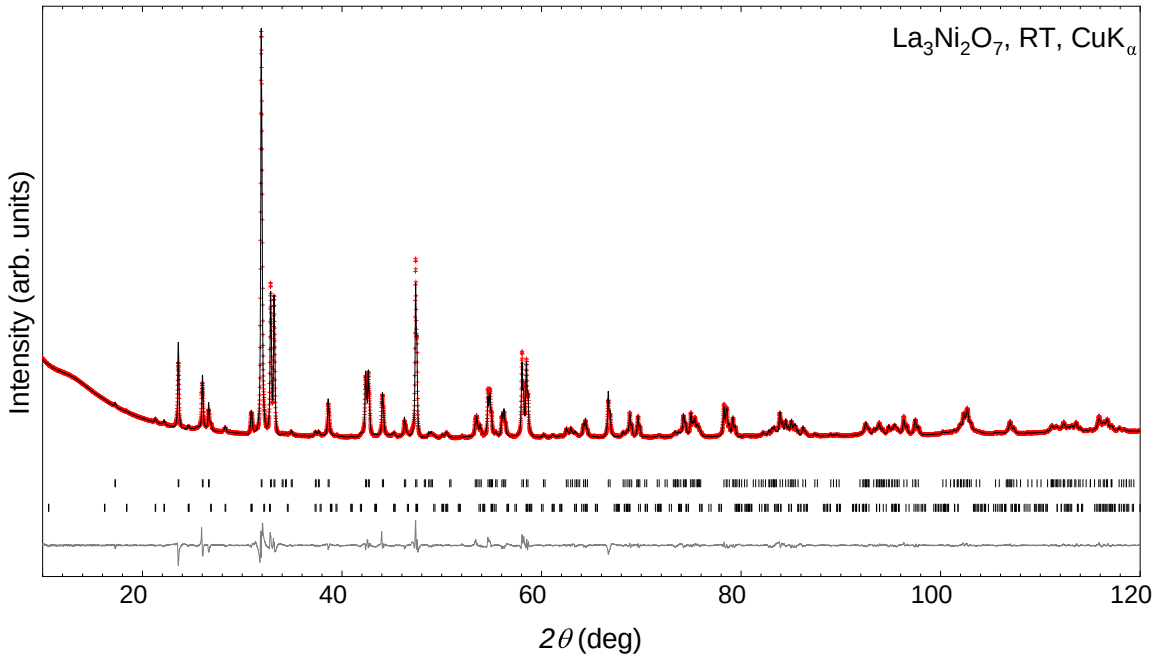

FIG. 1: Rietveld fit of powder x-ray diffraction data recorded at room temperature for $La_3Ni_2O_{7-\delta}$ sample. Red crosses: observed data. Black lines: calculated pattern. Grey lines: observed - calculated pattern. The vertical ticks indicate the positions of the Bragg reflections.

II. THE INCOMMENSURATE *VS.* COMMENSURATE MAGNETIC ORDER IN $LA_3NI_2O_{7-\delta}$

The μSR technique can distinguish between commensurate and incommensurate types of magnetic orders. Incommensurate order is characterized by a magnetic propagation vector that is not a rational factor of the crystallographic lattice parameters. This results in a very specific magnetic field distribution of the internal fields on the muon stopping site(s) ($B_{\rm int}$'s) which might be characterized either by a long tail from a maximum field down to $B = 0$ or by the appearance of a minimum and maximum fields with a broad plateau between them. The commensurate type of magnetic order is, in contrast, characterized by a single or several symmetric peaks (see, *e.g.*, μSR textbooks for further details, Refs. 7–13).

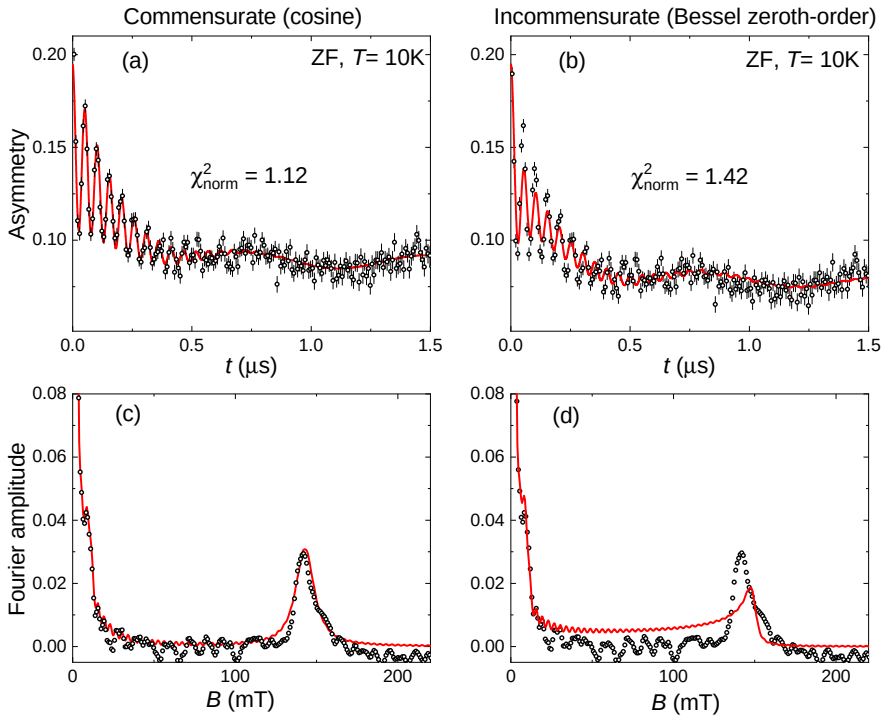

FIG. 2: (a) The zero-field μSR time spectra of the $La_3Ni_2O_{7-\delta}$ sample measured at ambient pressure $T = 10$ K. The red line corresponds to the fit within the 'commensurate' model (Eq. 1 with the magnetic part described by Eq. 2). (b) The same as in panel (a), but with the red line corresponding to the 'incommensurate' fit (Eq. 1 with the magnetic part described by Eq. 3). (c) The Fourier transform of the data presented in panel (a). (d) The Fourier transform of the data presented in panel (b).

Figure 2 shows the ZF-μSR response of $La_3Ni_2O_{7-\delta}$ measured at ambient pressure at $T = 10$ K. Panels (a)/(b) and (c)/(d) correspond to the ZF asymmetry spectra, representing the time evolution of the muon-spin polarization, and the Fourier transformations, showing the distribution of the internal fields, respectively. The difference between the two sets of panels corresponds to the 'commensurate' and 'incommensurate' types of data analysis procedure.

The fit to the experimental data was performed using Eq. 1 from the main paper:

$$A(t) = A_{\rm s}[f_{\rm m}P_{\rm s,m}(t) + (1 - f_{\rm m})P_{\rm s,nm}] + A_{\rm bg}P_{\rm bg}(t). \quad (1)$$

The commensurate (cm) and incommensurate (icm) data analysis procedures were performed using the decaying cosine and the zeroth-order Bessel (J_0) functions as:

$$P^{\rm cm}_{\rm s,m}(t) = \frac{2}{3}\sum_i f_i e^{-\lambda_{{\rm T},i}t}\cos(\gamma_\mu B_{{\rm int},i}t) + \frac{1}{3}e^{-\lambda_{\rm L}} \quad (2)$$

and

$$P^{\rm icm}_{\rm s,m}(t) = \frac{2}{3}\sum_i f_i e^{-\lambda_{{\rm T},i}t}J_0(\gamma_\mu B_{{\rm int},i}t) + \frac{1}{3}e^{-\lambda_{\rm L}}. \quad (3)$$

The fit results within the commensurate and incommensurate types of approaches are presented in Figs. 2 (a) and (b) by red solid lines. The 'commensurate' fit results in a better agreement with the experimental data, which is

also confirmed by a smaller value of the reduced $\chi^2_{\rm norm}$ [$\simeq 1.12$ compared with $\simeq 1.42$, Figs. 2 (a) and (b)]. The Fourier transform also results in the absence of a broad plateau in the direction to $B = 0$ as might be expected for the incommensurate type of magnetic order [compare the panels (c) and (d) of Fig. 2].

III. ADDITIONAL DATA FOR μSR UNDER PRESSURE STUDIES

Two representative WTF-μSR time spectra measured below ($T \simeq 10$ K) and above ($T \simeq 217$ K) the magnetic transition temperature are shown in Fig. 3 (a). The fit of WTF data was performed using Eq. 1 with the sample contribution described as:

$$P_{\rm s}(t) = f_{\rm m}\left[\frac{2}{3}e^{-\lambda_{\rm T}t} + \frac{1}{3}e^{-\lambda_{\rm L}t}\right] + (1-f_{\rm m})e^{-\sigma^2_{\rm WTF}t^2/2}\cos(\gamma_\mu B_{\rm WTF}t + \phi). \quad (4)$$

Here, ϕ is the initial phase of the muon-spin ensemble, $B_{\rm WTF} = 5$ mT is the weak transverse field, and $\sigma_{\rm WTF}$ is the Gaussian relaxation rate of the nonmagnetic component. The first term on the right-hand side of Eq. 4 is equivalent to Eq. 2, where, due to data binning, all the oscillating components can be combined into a single decay term. The second component describes the muon spin precession in $B_{\rm WTF}$ within the nonmagnetic phase.

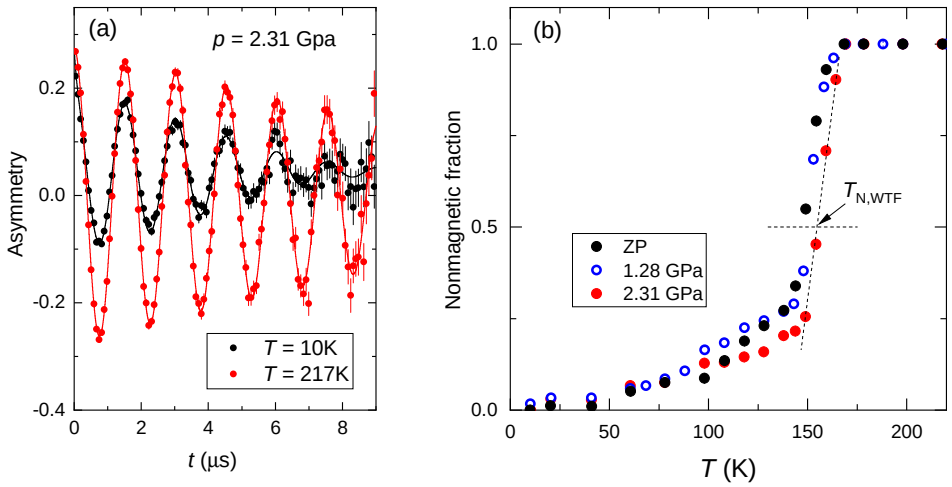

FIG. 3: (a) Weak transverse-field μSR time spectra measured below ($T = 10$ K) and above ($T = 217$ K) the magnetic transition ($T_{\rm WTF} \simeq 155$ K) at $p = 2.31$ GPa. (b) Temperature dependencies of the nonmagnetic fraction ($1 - f_{\rm m}$) obtained in weak transverse-field μSR experiments at pressures $p = 0.0$, 1.28, and 2.31 GPa.

The temperature dependencies of the nonmagnetic volume fraction ($1 - f_{\rm m}$) obtained in WTF-μSR experiments measured at applied pressures $p = 0.0$, 1.28, and 2.31 GPa, are plotted in Fig. 3 (b). The magnetic ordering temperature in WTF experiments ($T_{\rm N,WTF}$) was determined when half of the sample became nonmagnetic [$1 - f_{\rm m} = 0.5$, Fig. 3 (b)].

The ZF-μSR under pressure data were fitted similarly to that described in the ambient pressure case. For each pressure, the fit by means of Eq. 1 was performed globally, *i.e.*, by keeping the total magnetic fraction $f_{\rm m}$, the fraction of the 'slow precessing' component, and the ratio $B_{\rm int,Slow}/B_{\rm int,Fast}$ as a common parameter for each individual data set (see also Fig. 2 in the main text confirming that these parameters are nearly independent of T below $T_{\rm N}$). Note that in pressure experiments, a substantial portion of muons (more than 50%) are stopped in the pressure cell walls,[14,15] so the background contribution in Eq. 1 corresponds to the response of the pressure cell. The WTF and ZF responses of the pressure cell are generally studied in separated sets of experiments.[14–16]

IV. MUON STOPPING SITES

The muon stopping sites in $La_3Ni_2O_7$ were obtained by means of a DFT+μ approach[17] using the MuFinder application.[18] Density functional theory calculations were performed using the plane-wave pseudopotential code

CASTEP.[19] The generalised gradient approximation (PBE)[20] was used in all calculations. Calculations were converged to 0.5 meV/atom using a plane-wave cutoff of 900 eV and a $2 \times 2 \times 2$ k-point grid.[21] As has previously been done in this material,[22] we have applied an effective Coulomb interaction $U_{\text{eff}} = U - J = 4$ eV to the Ni $3d$ orbitals. A number of calculations were performed, each where a muon was implanted randomly into a supercell of approximately $11 \times 11 \times 21$ Å. The atomic positions were subsequently allowed to relax until the energy and atomic positions have converged to better than 5×10^{-3} meV/atom and 5×10^{-4} Å respectively, and the maximum force on any atom is less than 1×10^{-2} eV/Å. The final muon positions are clustered using the MuFinder application[18] to give the candidate muon stopping sites.

Site	**x**	**y**	**z**	**Energy (eV)**
1	0.495	0.006	0.170	0
2	0.465	0.035	0.019	0.33
3	0.362	0.000	0.227	0.35

TABLE I: The candidate muon stopping sites from DFT+μ analysis through MuFinder.[18] The fractional coordinates of the three crystallographically inequivalent sites are given for the conventional unit cell shown in the main text. The difference in energy between the DFT calculations is also shown.

We find three candidate muon sites where more than one calculation has converged to this muon position, see Table I. There are a few higher-energy configurations where the muon position is not reproduced in any other calculation, suggesting these are calculations that may have got stuck in a local energy minima and are unlikely to be occupied. The energy of the lowest energy candidate site is much lower than that of the other two; similarly, whilst there are no significant distortions to the crystal structure when the muon sits in the lowest energy candidate site, the distortions are more significant for the higher energy candidate sites, where a few La or Ni atoms have moved more than 0.2 Å. These distortions may well introduce a potential energy barrier that reduces the probability of these muon sites being occupied. Taken together, this suggests that it is most likely that the lowest energy candidate muon site is the only occupied site; this result is further supported by our magnetic dipole-field calculations.

V. DIPOLE-FIELD CALCULATIONS OF CANDIDATE MAGNETIC STRUCTURES

The candidate muon stopping sites were used in the MUESR code[23] to calculate the dipolar field at these sites for candidate magnetic structures. In such calculations, a classical dipole field source is placed on each Ni site, and the field at the muon site is subsequently calculated by summing the contribution from each of these sources. We used a crystallographic supercell of $2 \times 2 \times 1$ conventional cells for our calculations, which is sufficient to capture the magnetic unit cell, and the dipole field was calculated from a system of $20 \times 20 \times 20$ of these supercells. We assume there is no contribution to the field at the muon site from the Fermi contact hyperfine interaction. The magnetic structure in the $ab-$plane was based on those presented in Refs. 24,25, with the $c-$axis stacking then varied (exploring both ferro- and antiferro-magnetic coupling in this direction, as well as introducing stacking faults). Our results therefore provide an estimate of the maximum magnetic moment on the Ni site, as summarised in Table II.

The results presented in the main text are exclusively for the lowest energy candidate muon stopping site; whilst it represents a single crystallographic site, crystallographically-equivalent sites are sometimes magnetically-inequivalent, leading to multiple precession frequencies in the μSR spectra. In addition to the DFT arguments presented above, our dipole-field calculations also support the conclusion that the two higher energy candidate muon stopping sites are unoccupied. Both the higher energy candidate muon stopping sites give a significant contribution of fields at the muon stopping site between the low- and high-field peaks presented in the main text for a number of magnetic configurations. As this is not observed experimentally, it again suggests these sites are not occupied.

	Ni moment (μ_B)	
Zero moment Ni sites	$\perp$ c	$\parallel$ c
None	0.48 – 0.67	0.28 – 0.31
Single line	0.49 – 0.67	0.28 – 0.31
Double line	0.53 – 0.63	0.28 – 0.30

TABLE II: The possible values of the magnetic moment that are consistent with the μSR measurements, broken down by different magnetic configurations and orientation of the spins.

VI. CALCULATION OF THE SPIN SUSCEPTIBILITY

Here we calculate the spin susceptibility by using the multiorbital random phase approximation (RPA) taking into account on-site interactions above the magnetic transition.[26] We included an intraorbital interaction $U = 1.55$ eV and used the spin rotational invariance relations $U' = U - 2J_{\rm H}$ and $J' = J$ for the interorbital interaction U', Hund's coupling $J_{\rm H}$ and pair-hopping J'. The Hund's coupling was set to $J_{\rm H} = U/7$. In bilayer systems, when taking into account only hopping elements within a bilayer but not between bilayer sandwiches, the susceptibility can be decomposed in even and odd channels:[27]

$$\chi_{\rm spin} = \sum_{o_1,o_2} [\hat{\chi}^e_{o_1,o_2} \cos^2(\frac{q_z d}{2}) + \hat{\chi}^o_{o_1,o_2} \sin^2(\frac{q_z d}{2})]. \tag{5}$$

Here the summation is performed over all orbitals and different sublattices within the layer and d is the thickness of the bilayer sanwich. The RPA equations for even and odd channels can be separated and read:

$$\hat{\chi}^{(e/o)} = \left[\mathbb{1} - \frac{1}{2}\hat{\chi}_0^{(e/o)}\hat{U}^{(e/o)}\right]^{-1} \hat{\chi}_0^{(e/o)}. \tag{6}$$

The non-interacting susceptibilities can be connected to scattering between bonding (b) and antibonding (a) orbitals in the following way: $\hat{\chi}^e_0 = \hat{\chi}^{aa} + \hat{\chi}^{bb}$ and $\hat{\chi}^o_0 = \hat{\chi}^{ab} + \hat{\chi}^{ba}$.

The dominant peak in the susceptibility is connected to scattering between the bonding α and antibonding β bands, which is visualized in Fig. 4(f) of the main text. Note that the bonding γ band is below the Fermi surface within the tight-binding description by Wang *et al.*,[28] which is visualized in Fig. 4 (b). That description is derived from DFT calculations employing a hybrid functional for the exchange-correlation part, which shifts the γ band below the Fermi level (similar as from DFT+U calculations). For comparison we also investigated a different tight binding descriptions in which the γ pocket crosses the Fermi surface close to the Γ point. It is shown together with our computed band structure based on the local density approximation (LDA), using the same DFT package as in Ref. 29 in Fig. 4 (a). If the γ pocket is present at the Fermi surface, we find additional peaks in the spin susceptibility in which the largest contributions are connected to the scatterings involving the γ pocket. To obtain the largest contribution at $X_1 = (\pi/2, \pi/2)$ one would have to remove contributions from the γ band. The absence of the γ pocket at low temperatures and ambient pressure is also implied by ARPES measurements.[30] For the tight-binding model shown in Fig. 4(b) the peaks in the odd susceptibility are located at X_1. To perform the correct separation of the susceptibilities in the even and the odd channel we also added additional phase factor $e^{i\pi}$ between the two inequivalent atoms. This does not change the tight-binding dispersion but avoids artificial cancellations upon splitting the spin response into odd and even susceptibilities. The charge susceptibility is not shown explicitly but is similar to the spin susceptibility peaked at X_1 and dominated by the odd channel but is much smaller in magnitude.

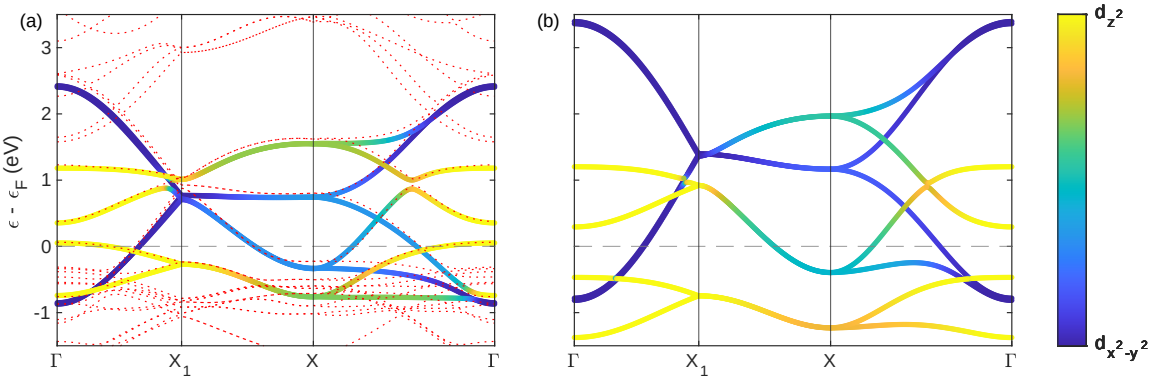

FIG. 4: (a) Downfolded tight binding bandstructure with orbital weights compared to complete LDA bandstructure (dotted red line) with γ band crossing the Fermi surface. (b) Tight binding model proposed in Ref. 28.

* Electronic address: rustem.khasanov@psi.ch

[1] H. M. Rietveld, *A profile refinement method for nuclear and magnetic structures*, J. Appl. Cryst. **2**, 65 (1969). https://doi.org/10.1107/S0021889869006558

[2] J. Rodríguez-Carvajal, *Recent advances in magnetic structure determination by neutron powder diffraction*, Physica B **192**, 55 (1993). https://doi.org/10.1016/0921-4526(93)90108-I

[3] Z. Zhang, M. Greenblatt, and J. B. Goodenough, *Synthesis, Structure, and Properties of the Layered Perovskite $La_3Ni_2O_{7-\delta}$*, J. Solid State Chem. **108**, 402 (1994). https://doi.org/10.1006/jssc.1994.1059

[4] V. Poltavets, Konstantin A. Lokshin, Takeshi Egami, and Martha Greenblatt, *The oxygen deficient Ruddlesden–Popper $La_3Ni_2O_{7-\delta}$ ($\delta = 0.65$) phase: Structure and properties*, Mater. Res. Bull. **41**, 955 (2006). https://doi.org/10.1016/j.materresbull.2006.01.028

[5] Ran Gao, Lun Jin, Shuyuan Huyan, Danrui Ni, Haozhe Wang, Xianghan Xu, Sergey L. Budko, Paul Canfield, Weiwei Xie, and Robert J. Cava, *Is $La_3Ni_2O_{6.5}$ a Bulk Superconducting Nickelate?*, arXiv:2311.11122. https://doi.org/10.48550/arXiv.2311.11122

[6] S. Lambert, A. Vincent, E. Bruneton, S. Beaudet-Savignat, F. Guillet, B. Minot, and F. Bouree, *Structural investigation of $La_{9.33}Si_6O_{26-}$ and $La_9AESi_6O_{26+\delta}$-doped apatites-type lanthanum silicate (AE =Ba, Sr and Ca) by neutron powder diffraction*, J. Solid State Chem. **179** 2602 (2006). https://doi.org/10.1016/j.jssc.2006.04.056

[7] A. Schenck, *Muon Spin Rotation Spectroscopy: Principles and Applications in Solid State Physics*, Adam Hilger, Bristol, 1985.

[8] A. Schenck and F.N. Gygax, *Magnetic Materials Studied by Muon Spin Rotation Spectroscopy*, in: Handbook of Magnetic Materials, edited by K.H.J. Buschow, Vol. 9, Pages 57-302 Elsevier, Amsterdam, 1995.

[9] V.P. Smilga and Yu.M. Belousov, *The Muon Method in Science*, Nova Science Publisher, 1994.

[10] E. Karlsson, *Solid State Phenomena, As Seen by Muons, Protons, and Excited Nuclei*, Clarendon, Oxford, 1995.

[11] S.L. Lee, S.H. Kilcoyne, and R. Cywinski (eds.), *Muon Science: Muons in Physics; Chemistry and Materials*, IOP Publishing, Bristol and Philadelphia, 1999.

[12] A. Yaouanc and P. D. de Réotier, *Muon Spin Rotation, Relaxation, and Resonance*, Oxford Science Publications, 2011.

[13] S. J. Blundell, R. De Renzi, T. Lancaster, F. L. Pratt (eds.) *Muon spectroscopy. An introduction*, Oxford: Oxford University Press, 2022.

[14] R. Khasanov, Z. Guguchia, A. Maisuradze, D. Andreica, M. Elender, A. Raselli, Z. Shermadini, T. Goko, F. Knecht, E. Morenzoni, and A. Amato, *High pressure research using muons at the Paul Scherrer Institute*, High Pressure Res. **36**, 140 (2016). https://doi.org/10.1080/08957959.2016.1173690

[15] Rustem Khasanov, *Perspective on muon-spin rotation/relaxation under hydrostatic pressure*, J. Appl. Phys. **132**, 190903 (2022). https://doi.org/10.1063/5.0119840

[16] Z. Shermadini, R. Khasanov, M. Elender, G. Simutis, Z. Guguchia, K.V. Kamenev, and A. Amato, *A low-background piston–cylinder-type hybrid high pressure cell for muon-spin rotation/relaxation experiments*, High Pressure Res. **37**, 449 (2017). https://doi.org/10.1080/08957959.2017.1373773

[17] S. J. Blundell and T. Lancaster, *DFT+ μ: Density functional theory for muon site determination*, Appl. Phys. Rev. **10**, 021316 (2023). https://doi.org/10.1063/5.0149080

[18] B.M. Huddart, A. Hernández-Melián, T.J. Hicken, M. Gomilšek, Z. Hawkhead, S.J. Clark, F.L. Pratt, and T. Lancaster, *MuFinder: A program to determine and analyse muon stopping sites*, Computer Physics Communications **280**, 108488 (2022). https://doi.org/10.1016/j.cpc.2022.108488

[19] Stewart J. Clark, Matthew D. Segall, Chris J. Pickard, Phil J. Hasnip, Matt I. J. Probert, Keith Refson, und Mike C. Payne, *First principles methods using CASTEP*, Z. Kristallogr. **220**, 567 (2005). https://doi.org/10.1524/zkri.220.5.567.65075

[20] John P. Perdew, Kieron Burke, and Matthias Ernzerhof, *Generalized Gradient Approximation Made Simple*, Phys. Rev. Lett. **77**, 3865 (1996). https://doi.org/10.1103/PhysRevLett.77.3865

[21] Hendrik J. Monkhorst and James D. Pack, *Special points for Brillouin-zone integrations*, Phys. Rev. B **13**, 5188 (1976). https://doi.org/10.1103/PhysRevB.13.5188

[22] Xuejiao Chen, Peiheng Jiang, Jie Li, Zhicheng Zhong, and Yi Lu, *Critical charge and spin instabilities in superconducting $La_3Ni_2O_7$*, arXiv:2307.07154. https://doi.org/10.48550/arXiv.2307.07154

[23] Pietro Bonfá, Ifeanyi John Onuorah, and Roberto De Renzi, *Introduction and a quick look at MUESR, the Magnetic structure and mUon Embedding Site Refinement suite*, JPS Conf. Proc. **21**, 011052 (2018). https://doi.org/10.7566/JPSCP.21.011052

[24] Xiaoyang Chen, Jaewon Choi, Zhicheng Jiang, Jiong Mei, Kun Jiang, Jie Li, Stefano Agrestini, Mirian Garcia-Fernandez, Xing Huang, Hualei Sun, Dawei Shen, Meng Wang, Jiangping Hu, Yi Lu, Ke-Jin Zhou, and Donglai Feng, *Electronic and magnetic excitations in $La_3Ni_22O_7$*, arXiv:2401.12657.

https://doi.org/10.48550/arXiv.2401.12657

[25] Tao Xie, Mengwu Huo, Xiaosheng Ni, Feiran Shen, Xing Huang, Hualei Sun, Helen C. Walker, Devashibhai Adroja, Dehong Yu, Bing Shen, Lunhua He, Kun Cao, and Meng Wang, *Neutron Scattering Studies on the High-Tc Superconductor* $La_3Ni_2O_{7-\delta}$ *at Ambient Pressure*, arXiv:2401.12635.
https://doi.org/10.48550/arXiv.2401.12635

[26] S. Graser, T. A. Maier, P. J. Hirschfeld and D. J. Scalapino, *Near-degeneracy of several pairing channels in multiorbital models for the Fe pnictides*, New J. Phys. **26** 023005 2009.
https://dx.doi.org/10.1088/1367-2630/11/2/025016

[27] Steffen Bötzel, Frank Lechermann, Jannik Gondolf, and Ilya M. Eremin, *Theory of magnetic excitations in multilayer nickelate superconductor* $La_3Ni_2O_7$, arXiv:2401.16151
https://arxiv.org/abs/2401.16151

[28] Yuxin Wang, Kun Jiang, Ziqiang Wang, Fu-Chun Zhang, Jiangping Hu, *Electronic structure and superconductivity in bilayer* $La_3Ni_22O_7$, arXiv:2401.15097.
https://doi.org/10.48550/arXiv.2401.15097

[29] F. Lechermann, J. Gondolf, S. Bötzel, and I. M. Eremin,*Electronic correlations and superconducting instability in* $La_3Ni_2O_7$ *under high pressure*, Phys. Rev. B **108**, L201121 (2023).
https://journals.aps.org/prb/abstract/10.1103/PhysRevB.108.L201121

[30] Jiangang Yang, Hualei Sun, Xunwu Hu, Yuyang Xie, Taimin Miao, Hailan Luo, Hao Chen, Bo Liang, Wenpei Zhu, Gexing Qu, Cui-Qun Chen, Mengwu Huo, Yaobo Huang, Shenjin Zhang, Fengfeng Zhang, Feng Yang, Zhimin Wang, Qinjun Peng, Hanqing Mao, Guodong Liu, Zuyan Xu, Tian Qian, Dao-Xin Yao, Meng Wang, Lin Zhao, and X. J. Zhou, *Orbital-Dependent Electron Correlation in Double-Layer Nickelate* $La_3Ni_22O_7$, arXiv:2309.01148.
https://doi.org/10.48550/arXiv.2309.01148